Nanoscale

Accepted Manuscript

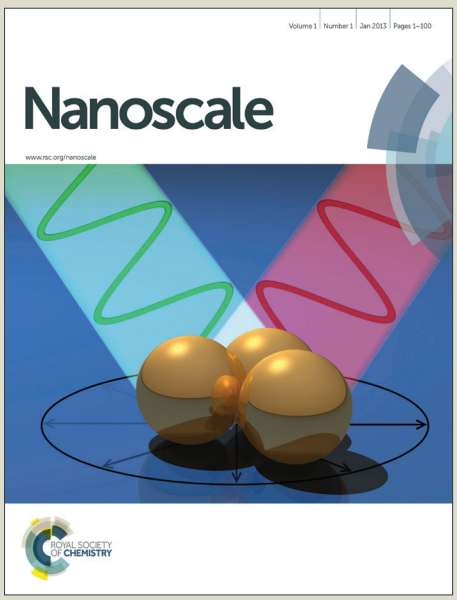

ROYAL SOCIETY OF CHEMISTRY

www.rsc.org/nanoscale

Manuscript Title:

Ag_3PO_4/nitridized $Sr_2Nb_2O_7$ composite photocatalyst with adjustable band structures for efficient elimination of gaseous organic pollutants under visible light irradiation

Jianjun Guo[a,b,c], Han Zhou[b,c], Shuxin Ouyang[d,*] , Tetsuya Kako[a,b], and Jinhua Ye[a,b,c,d,*]

[a] *Graduate School of Chemical Science, Hokkaido University, Sapporo, Japan.*

[b] *Environmental Remediation Materials Unit, National Institute for Materials Science (NIMS), 1-1 Namiki, Tsukuba, Ibaraki, Japan.*

[c]*International Center for Materials Nanoarchitectonics(WPI-MANA), National Institute for Materials Science (NIMS), 1-1 Namiki, Tsukuba, Ibaraki, Japan.*

[d]*TU-NIMS Joint Research Center, School of Materials Science and Engineering, Tianjin University, 92 Weijin Road, Nankai District, Tianjin, P. R. China.*

[*] Author to whom correspondence should be addressed.

Electronic mail:oysx@tju.edu.cn and Jinhua.YE@nims.go.jp.

Abstract:

A new heterojunction Ag_3PO_4/nitridized $Sr_2Nb_2O_7$ (N = 0~6.18 wt %) was designed to eliminate the gaseous pollutants under visible light irradiation. The phase compositions, optical properties, and morphologies of the heterojunction photocatalysts were systematically investigated via powder X-ray diffraction, UV-Visible absorption spectroscopy, scanning electron microscopy, energy-dispersive X-ray spectroscopy, and transmission electron microscopy. The calculation of electronic structure indicates that the top of the valance band of $Sr_2Nb_2O_7$ could be lifted up by nitrogen doping. Therefore, the electronic structure of Ag_3PO_4/nitridized $Sr_2Nb_2O_7$ composite photocatalysts could be continually changed by controlling amount of nitrogen in nitridized $Sr_2Nb_2O_7$. The photocatalytic degradation of Isopropyl alcohol (IPA) was carried out to test the photocatalytic activity of the heterojunction. The results indicated that the highest activity (CO_2 evolution rate, 10.32 $ppmh^{-1}$) was observed over the heterojunction of Ag_3PO_4/nitridized $Sr_2Nb_2O_7$, which was prepared by nitridation of SNO at 1023 K. The CO_2 evolution rate over the heterojunction was about 40 times higher than that of the pure Ag_3PO_4 (CO_2 evolution rate, 0.26 $ppmh^{-1}$) under visible light irradiation. An investigation of energy-band structure via valence-band X-ray photoelectron spectrum indicates that the conduction band (CB) and valence band (VB) of Ag_3PO_4 are both more positive than that of nitridized $Sr_2Nb_2O_7$ which facilitates the separation and transfer of photogenerated electrons and holes between the two photocatalysts. By continually adjusted the electronic structures, the optimal band gap of the nitridized $Sr_2Nb_2O_7$ is proved as

about 2.15 eV and the potential of valance band is +1.88 eV.

1. Introduction

Nowadays, the air pollution has become the most crucial issue around the world especially in the developing country. The photocatalytic degradation of the organic pollutants in the air has attracted increasing interests because it's a promising, environmental, and cost-effective technology [1-4]. During the past decades, great efforts have been made to exploit the efficient photocatalysts, such as TiO_2 and N-doped $TiO_{2-x}N_x$ [5-10], $AgNbO_{3(1-x)}SrTiO_{3(x)}$ [11,12], Na-based materials [13,14], Ag-based materials [15-18], WO_3[19], $PbSnO_3$[20] and etc[21]. Compared with the wide band gap photocatalyts, the visible- light sensitive photocatalysts can absorb more solar energy because of the narrower band structure. As one of the most efficient visible-light-sensitive photocatalysts, Ag_3PO_4 has been reported with a quantum efficiency of ~90% around 420 nm in water oxidation which indicates it has great potential in photocatalytic applications [22a]. Moreover, further investigations about the photoelectric/ photocatalytic properties, morphology controlling, and facet effect of Ag_3PO_4 were carried out, and enhanced performances were obtained [22 b,c,d,e]. However, the photoactivities of Ag_3PO_4 in photodecomposition of gaseous organic contaminants are still worth to further improve. One reason is that its potential of the conduction band (CB) is more positive than the reduction potential of O_2 ($e^- + O_2 + H^+ \rightarrow HO_2$, -0.046 V vs NHE) [23, 24]. As a result, the generated electrons cannot be consumed by combining with O_2 which is very important for the photooxidization of the gaseous organic compound [25]. Another reason is that the decomposition of IPA

to CO_2 is a complex multielectron-involved process ($CH_3CHOHCH_3 + 5H_2O + 18h^+ \rightarrow 3CO_2 + 18H^+$) [26a], which is difficult to be realized on pure Ag_3PO_4. Moreover, as the electrode potential of Ag_3PO_4/Ag (around 0.45 V vs. NHE) is more positive than that of H^+/H_2 (0 V vs. NHE) [26b], Ag_3PO_4 can easily be reduced to Ag^0 during in the photocatalytic reactions.

Recently, a new composite photocatalysts based on Ag_3PO_4 and Cr doped $SrTiO_3$ has been successfully synthesized with enhanced photoactivity[27]. It was found that electronic structures of composite photocatalyst promote the generation and separation of photo-generated electron-hole pairs and the multi-electron reactions. As a result, the composite photocatalyst exhibited much higher activity than the individual Ag_3PO_4 and Cr-doped $SrTiO_3$. However, there is a remained problem that the oxidization potential of the holes would be lowered after transferring. Therefore, to find an optimal balance between the transfer of electron/holes pairs and the redox potentials is an important issue for improving the photocatalytic activity of composite photocatalysts.

Herein, another Sr-based semiconductor (nitridized $Sr_2Nb_2O_7$) with adjustable band gaps was chosen as the candidate for a new composite photocatalyst Ag_3PO_4/nitridized $Sr_2Nb_2O_7$ for efficient photodegradation of organic pollutants. $Sr_2Nb_2O_7$ as a wide band-gap semiconductor has attracted wide interest because of its high quantum yields for the overall photocatalytic water splitting [28-35]. Moreover, doping of foreign elements is a strategy to develop visible-light efficient photocatalysts. Recently, nitridized $Sr_2Nb_2O_7$ has been exploited with much narrower

band gap for water splitting under the visible light irradiation [36-38]. In this study, we synthesized composite photocatalysts based on the Ag_3PO_4 and the nitridized $Sr_2Nb_2O_7$ with adjustable band gaps from a $Sr_2Nb_2O_7$ precursor by nitridation with NH_3 under different temperatures. Iso-propanol (IPA) photodegradation over the heterojunctions under visible-light irradiation was employed for evaluating their photocatalytic properties. The valence-band state of Ag_3PO_4 and nitridized $Sr_2Nb_2O_7$ were analyzed by X-ray photoelectron spectroscopy (XPS) and the DOS calculation, which helps find the optimal band structure for the best photocatalytic activity.

2. Experimental

2.1 Photocatalysts preparation. All of the reagents were analytical grade and used without further purification. nitridized $Sr_2Nb_2O_7$ were obtained by nitriding the $Sr_2Nb_2O_7$ precursor, which synthesized by the polymerized complex method as previously report [38]. In a typical synthesis, $NbCl_5$ (High Purity Chemicals, 99.9%) and strontium acetate ($Sr(Ac)_2$•$0.5H_2O$) (Wako Pure Chemical, 99.0%) were dissolved in a stoichiometric ratio in methanol. Citric acid (Wako Pure Chemicals, 98.0%) and ethylene glycol (Wako Pure Chemical, 99.5%) were added, and the solution was kept at 473 K overnight to promote polymerization. After becoming a yellow resin, the mixture was pyrolyzed at 623 K, followed by calcination in air at 923 K and 1073 K for 2 h each, with intermediate grinding. The obtained white oxide powder was then nitrided under NH_3 flow (500 $mL \cdot min^{-1}$) for 3 h at 873K, 923K, 973K, 1023K, 1073K, and 1173 K in a quartz tube reactor. After nitridation, the catalysts were cooled to room temperature under He flow to remove adsorbed NH_3 molecules on the surface.

The color of the catalysts obtained after nitridation varied from white to dark brown with increasing nitridation temperatures. After-treatment was carried out in atmosphere at 673K for 2 h to reduce the defect. The production of nitridized $Sr_2Nb_2O_7$ was confirmed by X-ray diffraction analysis. The obtained nitridized $Sr_2Nb_2O_7$ named as SNON-873, SNON-923, SNON-973, SNON-1023, SNON-1073, and SNON-1173 for the samples were nitrided under 873K, 923K, 973K, 1023K, 1073K, and 1173K, respectively. The Ag_3PO_4 was synthesized by the ion-exchange method as described in our former report [25]. Appropriate amounts of $AgNO_3$ and Na_2HPO_4 were mixed and milled thoroughly until the initial color changed to yellow. The obtained precipitate was washed with distilled water for several times and dried at room temperature overnight. The Ag_3PO_4/nitridized $Sr_2Nb_2O_7$ heterojunctions were prepared by grinding and mixing individual solids thoroughly in ethanol in an agate mortar. After that, the prepared samples were dried at 60°C and then calcined at 673K for 2h in an oven to construct composite structure.

2.2 Photocatalysts characterization.

The crystal structure of the catalysts obtained was determined a Rigaku Rint-2000 X-ray diffractometer equipped with graphite monochromatized Cu-Kα radiation (λ=1.54178 Å). Scanning electron microscopy images and energy-dispersive X-ray spectroscopy patterns were recorded with a JEOL 6700F field emission scanning electron microscope. Transmission electron microscop and high-resolution images were performed with a JEOL 2100F field emission transmission electron microscope operated at 200 kV. Absorption properties were analyzed by UV-visible diffuse

reflectance spectroscope (UV-Vis DRS, Shimadzu, UV-2500) and converted to absorption spectra by the standard Kubelka-Munk method. Elemental analysis of oxynitride samples were carried out by a TCD measurement EMGA-920. The surface area measurements were carried out in a Surface Area Analyzer (BELSORP II). The relative positions of the valence band tops of Ag_3PO_4 and nitridized $Sr_2Nb_2O_7$ were investigated by an X-ray photoelectron spectroscopy (PHI Quantera SXM).

2.3 Theoretical calculations.

Electronic structures of the $Sr_2Nb_2O_7$ and $SrNbO_2N$ were investigated via the plane-wave-pseudopotential approach based on the density functional theory (DFT). Geometry optimization model was performed to determine the most stable structures. Then its electronic structure was calculated using a standard Cambridge serial total energy package (CASTEP) code [39,40]. The electron-core interaction was represented via ultrasoft pseudo potentials with a plane-wave basis cutoff energy of 340 eV. The electronic exchange-correlation energy was treated within the frame-work of the local density approximation (LDA). The self-consistent field (SCF) tolerance was all 1×10^{-6} eV/atom.

2.4 Photocatalytic reaction.

In the photocatalytic measurement, a 300 W Xe arc lamp (7 A imported current, focused through a 45 × 45 mm shutter window) equipped with a set of glass filters (L42 + HA30, 420 nm < λ < 800 nm, HOYA.CO.,JAPAN) and a water filter was used as the light source. Under such condition, the illumination intensity was about 30.5mWcm^{-2}. The 0.2 g of sample was evenly spread over a dish with an area of 8.5

cm^2 in a 500 mL of a borosilicate glass vessel. Then the inside atmosphere of the vessel was exchanged by artificial air [V (N_2) : V(O_2) = 4 : 1] for 10 min to remove gaseous impurities. After the sample was sealed in the vessel, gaseous isopropyl alcohol (IPA) was injected into the vessel (the initial concentration of IPA was about 1250 ppm ~ 1500 ppm). Before irradiation, the sample was kept in the dark to ensure an adsorption-desorption state of IPA on the sample. The final products of the photocatalytic oxidation of IPA were CO_2 and H_2O. To evaluate the photocatalytic activity, the IPA and CO_2 were measured by using a gas chromatography (GC-2014, Shimadzu Corp., Japan) equipped with a methanizer and a flame ionization detector (FID).

3. Results and Discussion

3.1 Physical properties and band structures of the $Sr_2Nb_2O_7$-nitrides

Fig. 1 shows X-ray diffraction (XRD) patterns of nitridized $Sr_2Nb_2O_7$. The XRD pattern for $Sr_2Nb_2O_7$, prepared as the parent oxide, is consistent with that for layered perovskite type $Sr_2Nb_2O_7$ [41,42]. Meanwhile, the XRD pattern of oxynitride (nitrided at 1173K) is in agreement with the reported cubic structure of $SrNbO_2N$. The intensity of diffraction peaks of the orthorhombic phase decreased with nitridation temperature and later completely disappeared at 1173 K. On the contrary, the diffraction peaks of cubic phase (oxynitrides) were observed even at 973 K, and their intensity increased with nitridation temperature. The results reveal the possibility of co-existence of the $Sr_2Nb_2O_7$ and $SrNbO_2N$ phases. The effect of each phase on band-gap will be discussed latter. The XRD pattern of sample nitrided at 1173 K

shows that this sample with no impurity phase and this pattern is consistent with that of the cubic phase of $SrNbO_2N$. Thus we conclude that nitrogen doping of the pure layered oxide catalyst transforms the orthorhombic $Sr_2Nb_2O_7$ structure to the cubic oxynitride $SrNbO_2N$.

Elemental analysis of oxynitride samples indicates that nitrogen was doped in the samples with different content (see Table 1). Elemental analysis of oxynitride samples indicates the stoichiometry of nitridized $Sr_2Nb_2O_7$ (N: 0~6.18 wt%), with higher nitrogen amount at higher nitridization temperatures. Meanwhile, it's worth to mention that the nitrogen amount of SNON-1173 is a little less than that of $SrNbO_2N$ (6.18 wt% < 6.8 wt%), which due to the N cannot be doped ideally. However, it doesn't affect that the sample was considered as $SrNbO_2N$ as shown in XRD patterns.

Fig. 2 shows UV-Vis diffuse reflectance (DR) spectra of the pure oxide and nitridized samples prepared at different nitridation temperatures. The absorption spectrum of $Sr_2Nb_2O_7$ indicates that it can absorb solar energy with a wavelength shorter than ~300 nm. The increase in nitridation temperature shifted the photon absorption of the photocatalysts into the visible range. The pure oxide showed the absorption only in the UV region (~300 nm), whereas nitridized samples showed increased and extended absorption in the range of 350 ~ 600 nm. There was a slight red-shift of the main absorption peak, but the visible light absorption appeared mostly as a shoulder to the main peak. All nitride samples absorbed light in the visible region, although the level of background absorption was high, probably owing to the production of reduced Nb species (e.g., Nb^{3+} and Nb^{4+}) during nitridation [36]. In

accordance, the colour of the sample is changed from white to deep red belong with the nitridation temperature increasing.

Furthermore, the band gaps of the as-prepared samples were obtained based on the calculation of band-structure. For a crystalline semiconductor, the optical absorption near the band edge can be described by the equation [17]:

$$(\alpha h\nu)^n = A(h\nu - E_g)$$

Where α, ν, A, h, and E_g represent the absorption coefficient, light frequency, proportionality constant, plank constant and band gap, respectively. In the equation, *n* depends on the transition characteristic of the photocatalyst. For an indirect semiconductor, *n* equals 0.5, while *n* is 2 for a direct semiconductor. The the (ahν) versus the band energy is shown in Fig. 2 (b).

For a direct observation, the experimental band-gaps are listed in Table 1 and shown in Fig. 3. We can find that the band gaps of the nitridized $Sr_2Nb_2O_7$ were narrowed along with the nitridation temperature increasing. It has to notice that two phases are coexisted. However, due to the band gap of $SrNbO_2N$ is settled, the reason for the band-gap narrowing of nitridized $Sr_2Nb_2O_7$ is mainly attributed to the contribution of orthorhombic phase.

The optical absorption property of a photocatalyst is largely dependent on the band structure, thus the theoretical calculation of the band structure helps understanding its photophysical and photocatalytic properties [23]. The $Sr_2Nb_2O_7$ and the $SrNbO_2N$ were chosen as the examples. The corresponding crystal structures of pure $Sr_2Nb_2O_7$ and $SrNbO_2N$ are illustrated in Fig. 4. The oxide $Sr_2Nb_2O_7$ is a (110)

layered perovskite of the Carpy and Galy type with a space group of Cmc21, and an orthorhombic unit cell with lattice parameters of a =3.930 Å ,b = 26.726 Å, c= 5.683 Å[39], while oxynitride $SrNbO_2N$ is a non-layered cubic structure with a space group of Pm3m, a =b = c = 4.044 Å.

Based on the crystal structure, the band-structure was calculated by DFT. As shown in the Fig. 5 (a,c), the electronic calculation indicates that $Sr_2Nb_2O_7$ and $SrNbO_2N$ are indirect and direct band gap semiconductor, respectively. Moreover, the energy-band calculation indicates that the deduced band-gap of the $SrNbO_2N$ (Eg = 1.1 eV) is much narrower than that of the $Sr_2Nb_2O_7$ (Eg = 2.8 eV).

In order to confirm the reason of band narrowing, the total and projected partial densities of states (DOS) of the $Sr_2Nb_2O_7$ and $SrNbO_2N$ are investigated, where the top of the valence band was set to 0 eV. As shown in Fig. 5 (b,d), the states at top of valence band for $Sr_2Nb_2O_7$ was contributed by O 2p orbitals. Moreover, the states at conduction band minimum are the contribution of Nb 4d, which is in accordance with previous report. For the $SrNbO_2N$, the major contribution in the top of valence band comes from O 2p hybridized with N 2p orbitals. It is clear from DOS studies that the band-gap gets narrowed due to mixing N 2p with O 2p orbitals from nitrogen doping. The N 2p orbitals have higher potential energies than O 2p orbitals [38], and so their hybridization lifts up the top of the valence band from the position of the $Sr_2Nb_2O_7$, which also makes the material to shift the optical absorption into the visible light region (as illuminated in Fig.3).

Moreover, the conduction band bottoms of $Sr_2Nb_2O_7$ and $SrNbO_2N$ are

significantly different. As shown in the Fig. 5 (a,c), the potential of conduction band bottom in $Sr_2Nb_2O_7$ is higher than that in $SrNbO_2N$. The reason may be due to the variant octahedral ligand field of $Sr_2Nb_2O_7$ which changes Nb-O bond lengths and O-Nb-O bond angels (as listed in Table 2) of the basic cubic crystal structure of the $SrNbO_2N$. The tilts of Nb-O bonds and the shifts of bond lengths contribute to lower the energy of the conduction band bottom when crystal structure changes from the orthorhombic of $Sr_2Nb_2O_7$ to the cubic of $SrNbO_2N$ (as illuminated in Fig.5).

Moreover, the calculated band-gaps of the samples are significantly small than the experimental results. For instance, the calculated band gap of $Sr_2Nb_2O_7$ is about 2.8 eV (see Fig.5a) which is narrower than the experimental band gap 3.96 eV. This is understandable since the band gap calculated by DFT is generally smaller than the experimental result, which is considered as a feature of the DFT calculation [43].

3.2 Characterizations and photoactivities of the Ag_3PO_4/nitridized $Sr_2Nb_2O_7$ composite photocatalysts under visible light irradiation

The Ag_3PO_4/nitridized $Sr_2Nb_2O_7$ (N:0~6.18 wt%) composite photocatalysts were synthesized via solid state reaction.

Fig. 6 (a) shows the XRD pattern of the single photocatalysts and composite photocatalysts. The indexed diffraction peaks can be ascribed as Ag_3PO_4, $Sr_2Nb_2O_7$, and $SrNbO_2N$, respectively. Peaks related to other niobates were not observed in the synthesized samples, indicating that the single photocatalysts didn't react with each other. As shown in Fig. 6 (b), the TEM image of the SNON-1023 reveals that it belongs to layered material which is accordance with previouse report [38]. Moreover,

Fig. 6 (c) shows that two materials are well connected, which is advantageous for the inter-particle photocarrier transfer between Ag_3PO_4 and SNON-1023. Fig.6 (d) shows the UV-Vis absorption spectra of Ag_3PO_4, SNON-1023, and Ag_3PO_4/ SNON-1023 composite. The absorption spectrum of Ag_3PO_4 indicates that it can absorb solar energy with a wavelength shorter than ~530 nm. Moreover, the two absorption edges reveal an indirect band gap of 2.36 eV and a direct transition of 2.43 eV, which are generally in agreement with our previous work [22]. Meanwhile, the light absorption of SNON-1023 is obviously weaker than that of Ag_3PO_4 below 500 nm, but stronger in the region above 500 nm. As a result, the heterojunction exhibits stronger absorption over 500 nm than that of Ag_3PO_4.

Gaseous Isopropyl alcohol (IPA) was chosen as a model pollutant for the evaluation of photocatalytic activities of the Ag_3PO_4/nitridized $Sr_2Nb_2O_7$ composite photocatalysts. The photocatalytic conversions of IPA to CO_2 over different photocatalysts were carried out under visible light irradiation (420 nm<λ<800 nm). As shown in Fig.7, all of the individual photocatalysts exhibit lower activities with comparison of composite photocatalysts. The evolution rates of acetone and CO_2 of the $Sr_2Nb_2O_7$ are about 5.2 $ppmh^{-1}$ and 0.49 $ppmh^{-1}$, respectively. It is understandable that the wide band gap of $Sr_2Nb_2O_7$ make it unable to absorb visible light. For the nitridized $Sr_2Nb_2O_7$ obtained at different temperatures, the evolution rates of acetone and CO_2 are also very low. It seems that although the nitridized $Sr_2Nb_2O_7$ can absorb more visible light, the generated electrons/holes may tend to recombine easily due to their narrowed band gap. The reason for the low activity of Ag_3PO_4 can be explained

as we previously reported [17], which is attributed to the redox potentials of electrons and holes. After constructing the composite photocatalysts, all of the composite photocatalysts exhibited higher photoactivity than the individual material. In comparison, the Ag_3PO_4/SNON-1023 composite photocatalyst exhibited best activity with the evolution rates of acetone and CO_2 are about 173.3 $ppmh^{-1}$ and 10.32 $ppmh^{-1}$, which is significantly higher than that of other composite photocatalysts. When nitridation temperature < 1023K, the evolution rates of acetone and CO_2 increase; however, when the nitridation temperature > 1023K, the evolution rates of acetone and CO_2 decreases.

To investigate the activity in more details, the degradation of IPA over time for Ag_3PO_4/SNON-1023 and pure photocatalysts were analyzed (Fig. 8a). In the presence of Ag_3PO_4/SNON-1023 sample, 96% of the IPA is degraded within 6.5 h of irradiation. In contrast, the IPA decomposition ratios are 4.8 % and 36.3 % over pure Ag_3PO_4 and SNON-1023 after 10 h of irradiation, respectively. Moreover, as shown in Fig. 8b, the amount of CO_2 evolution over Ag_3PO_4/SNON-1023 is much higher than that of pure SNON-1023 and Ag_3PO_4 respectively. There is 284.1 ppm of CO_2 obtained by Ag_3PO_4/SNON-1023, but 7.7 ppm and 66.8 ppm were achieved by Ag_3PO_4 and SNON-1023, respectively. The evolution of acetone was also investigated. As shown in Fig.8c, the Ag_3PO_4/SNON-1023 exhibits the highest activity in acetone evolution (about 173.3 $ppmh^{-1}$) in the first 6.5 h irradiation. After that, the evolution curve got highest peak which means that all of the IPA was degraded into acetone and CO_2. In comparison, the Ag_3PO_4 and the SNON-1023 exhibited much lower activity with the

rate about 4.8 ppmh^{-1}and 17.8 ppmh^{-1}, respectively.

Moreover, the overall reaction of the deep photocatalytic oxidation of IPA to CO_2 is shown as below:

$$CH_3CHOHCH_3 + 5H_2O + 18h^+ \rightarrow 3CO_2 + 18H^+$$

Therefore, the AQE of the photocatalyst in IPA photodecomposition could be calculated by the equation:

$$\mathbf{AQE = [[N(CO_2) \times 6 + N(acetone)] / N (photons)] \times 100\ \%}$$

In which, [N(CO_2)] and N(acetone)] signify the mole number of generated CO_2 and generated acetone in unit time; [N (photons)] signify the number of incident photons in unite time;

In this work, the AQE of the Ag_3PO_4/nitridized $Sr_2Nb_2O_7$ (N:2.42 wt%) were calculated as 0.13%.

3.3 The mechanism for the enhanced activity

Since photocatalytic activity is largely dependent on the band structure, the investigations of conduction band (CB) and the valence band (VB) are necessary for understanding the enhanced photocatalytic activity [37~40]. As we previously reported, a good matching of the CB and VB levels of the composite photocatalysts can realize the vectorial transfer of photogenerated charge carriers from one photocatalyst to the other, which can contribute to improving the photocatalytic efficiency [41]. Therefore, we also compared the relative position of the VB tops of the Ag_3PO_4 and SNON-1023 via their VB X-ray photoelectron spectroscopy (XPS) spectra.

As shown in Fig. 9 the VB top of Ag_3PO_4 is 1.02 V higher than that of SNON-1023. As we previously reported [25, 26], the band gap of Ag_3PO_4 is 2.45 eV, and its CB and VB positions are +0.45 eV and +2.90 eV (vs. NHE), respectively. Considering the band gap of SNON-1023 is about 2.15 eV (see Table 2), the potentials of VB and CB are thus +1.88 eV and -0.27 eV, respectively.

As illuminated in Fig.10, the potential difference between corresponding energy-band edges can drive the charge carriers from one material to its neighbor to form a spatial separation between electrons and holes. And then, the electrons and holes were aggregated which is advantageous for the multi-electron reactions.

On the other hand, the photocatalytic activities of other composite photocatalysts are much lower than that of Ag_3PO_4/SNON-1023 composite photocatalyst. This might be related to the redox potential of generated holes. Although the band structure of the composites would promote the separation of electrons/holes pairs, the redox ability of holes would be lowered after transferring due to the position of the valence band of the nitridized $Sr_2Nb_2O_7$. When the band gap of nitridized $Sr_2Nb_2O_7$ is wider than 2.15 eV, the position of the valence band is more positive than that of SNON-1023 which lowered the efficiency of holes transferring (also need to consider the decrease in visible light absorption); when the band gap of nitridized $Sr_2Nb_2O_7$ is narrower than 2.15 eV, the position of the valence band is so high that the redox potential of transferred holes is lowered and the recombination of electron/hole pairs is enhanced. Therefore, the optimal band gap is of the nitridized $Sr_2Nb_2O_7$ is around 2.15 eV which can make the balance between the separation of electron/hole pairs and the redox

potential of holes. Moreover, the surface areas of the samples were also measured by nitrogen adsorption method. As shown in Table 2, there is no obviously difference between each sample which excludes the effects of the surface area on the photoactivity.

4 Conclusions

A new heterojunction based on Ag_3PO_4 and nitridized $Sr_2Nb_2O_7$ was designed to attain the efficient elimination of gaseous IPA under visible light irradiation. The study of the electric structure indicates that the valance band of nitridized $Sr_2Nb_2O_7$ was lifted up due to mixing N 2*p* with O 2*p* orbitals from nitrogen doping which result in narrower band gap. Moreover, the band gap could be continually adjusted by the nitridation with NH_3 under different temperatures. The photocatalytic characterizations indicated that all of these composite photocatalysts exhibited higher efficiency than the individual samples under visible light-irradiation; in particular, the Ag_3PO_4/ nitridized $Sr_2Nb_2O_7$ (N: 2.42 wt%) composite photocatalyst showed the highest catalytic performance (CO_2 evolution rate, 10.3 $ppmh^{-1}$). The results reveal that the relative potentials of the valance band and the conduction band between the Ag_3PO_4 and the nitridized $Sr_2Nb_2O_7$ has significant effects on the photoactivity, and the optimal band gap of the nitridized $Sr_2Nb_2O_7$ is about 2.15 eV and the potentials of VB and CB are thus +1.88 eV and -0.27 eV, respectively. The present work is evidences that fabricating heterojunctions with proper hand structure to establish a new chemical reaction process is an effective strategy to enhance photocatalytic efficiency or attain new photocatalytic application. The results and discussions herein

supply useful informations for further developing the other heterojunction photocatalysts.

Reference

[1]Gaya, U. Ibrahim, Abdullah, A. Halim, J. Photochem, Photobiol. C: Photochem. Rev., 2008,9,1-12.

[2]H. Tong, S. X. Ouyang, Y. P. Bi, N. Umezawa, M. Oshikiri, Ye, J. H. Adv. Mater. 2012, 24, 229.

[3]S.Wang, H. M. Ang, M. Tade, Environ. Int. 2007, 33, 694-705.

[4]K. Demeestere, J. Dewulf, L.Van, Criti. Revie. Environ. Sci. Tech. 2007, 37, 489-538.

[5]F. Arsac, D. Bianchi, J. M. Chovelon, et al, J. Phys. Chem. A, 2007, 124, 149-155; F. Arsac, D. Bianchi, J. M. Chovelon, et al, J. Phys. Chem. A, 2006, 110, 4213-4222;

[6]D. Vildozo, C. Ferronato, S. Mohamad; et al, Appl. Catal. B- Environ., 2010, 94, 303-310.

[7]M. A. Henderson, N. A. Deskins, R. T. Zehr, et al. J. Catal., 2011, 279, 205-212.

[8]H. Choi, A. C. Sofranko, D. D. Dionysiou, Adv. Funct. Mater., 2006, 16, 1067-1074.

[9]C. C. Pan, J. Wu, C. S. Jeffrey, Mater. Chem. Phys., 2006, 100, 102-107.

[10]C. Chen, H. Bai, C. Chang, J. Phys. Chem. C., 2007,111,15228-15235.

[11]G. Li, T. Kako, Tetsuya; D. Wang, et al. J. Solid. State. Chem., 2007, 180, 2845-2850; G. Li, D. Wang, Z. Z. Zou, et al. J. Phys. Chem. C., 2008, 112, 20329.

[12]D. Wang, T. Kako, J. H. Ye, J. Phys. Chem.C, 2009, 113, 3785-3792.

[13]H. Shi, X. Li, H. Iwai, et al, J. Phys. Chem. Sol., 2009, 70, 931-935.

[14]T. Kako, Z. Z. Zou, M. Katagiri, et al., Chem. Mater., 2007, 19, 198-202.

[15]F. Shi, Z. Li, J. Kou, J. H. Ye, and Z. Zou, J. Phys. Chem. C., 2011, 115, 145-151.

[16]S. X. Ouyang, Z. S. Li, Z. Ouyang, et al. J. Phys. Chem. C., 2008, 112, 3134-3141.

[17]Q. Zhu , W. S. Wang , L. Lin , G. Q. Gao , H. L. Guo , H. Du , and A. W. Xu . J. Phys. Chem. C, 2013, 117, 5894–5900.

[18]G. Q. Li, T. Kako, D. Wang, et al, Dalton. Trans., 2009, 13, 2423-2427.

[19]D. Chen, J. H. Ye, Adv. Funct. Mater., 2008, 18, 1922-1928.

[20](a)D. Chen, S. X. Ouyang, J. H. Ye, Nano. Res. Lett., 2009, 4, 274-280.; (b)Q. Y. Li, T. Kako, J. H. Ye, Chem. Commun., 2010, 46, 5352-5354.

[21]H. F. Shi, Z. S. Li, J. H. Ye, et al. J. Phys. D- Appl. Phys., 2010,43.

[22](a). Z.G. Yi, J. H. Ye, K. Naoki, K. Tetsuya, et al, Nature Mater., 2010, 9, 5352. (b). J. J. Guo, S. X. Ouyang, H. Zhou,T. Kako, J. H. Ye, J. Phys. Chem. C, 2013, 117 (34), 17716–17724.(c) J. J. Guo, S. X. Ouyang, T. Kako, J. H. Ye, Appl. Sur. Sci., 2013, 280,418-423. (d). Y. P. Bi, J. H. Ye,et al. J. Mater. Chem. 2012, 22, 14847. (e). Y. P. Bi, J. H. Ye,et al. J. Am. Chem. Soc. 2011, 133, 6490.

[23]N. Umezawa, S. X. Ouyang, J. H. Ye, Phys. Rev. B, 2011, 83.

[24]A. J. Bard, R. Parsons, J. Jordan Standard Potentials in Aqueous Solution, CRC press (1985).

[25]S. X. Ouyang, J. H. Ye, J. Am. Chem. Soc., 2011, 133, 7757.

[26] Girish Kumar .S. and Gomathi Devi.L., J. Phys. Chem. A., 2011, 115, 13211.

[27] J.J. Guo, S. X. Ouyang, P. Li, Y. J. Zhang, T. Kako, J. H. Ye, Appl. Catal. B-Environ., 2013,134– 135, 286– 292.

[28]E. D. Jeong, M. G. Ha, M. S. Won, H. G. Kim, H. K. Pak, P. H. Borse, S. M. Ji and J. S. Lee, J. Korean Phys. Soc., 2006, 49, S671.

[29]H. G. Kim, D. W. Hwang, J. Kim, Y. G. Kim and J. S. Lee, Chem. Commun., 1999, 1077–1078.

[30]T. Takata, Y. Furumi, K. Shinohara, A. Tanaka, M. Hara, J. N. Kondo and K. Domen, Chem. Mater., 1997, 9, 1063.

[31]J. Kim, D. W. Hwang, H. G. Kim, S. W. Bae, J. S. Lee, W. Li and S. H. Oh, Top. Catal., 2005, 35, 295.

[32]Y. Kim, YI; P. M. Woodward, K. Z. Baba-Kishi, et al. Chem. Mater., 2004, 16, 1267

[33]D. Chen, J. H. Ye, Chem. Mater., 2009, 21, 2327-2333.

[34]K. Domen, J. Yoshimura, T. Sekine, A. Tanaka. et al., Catal. Lett., 1990, 4, 339.

[35]K. Sayama, A. Tanaka, K. Domen, K. Maruya and T. Onishi, J. Catal., 1990, 124, 541–547.

[36]B. Siritanaratkul, K. Maeda, T. Hisatomi, and K. Domen, Chem.Sus.Chem., 2011, 4, 74–78.

[37]K. Maeda, M. Higashi, B. Siritanaratkul, R. Abe, and K. Domen, J. Am. Chem. Soc. 2011, 133, 12334–12337.

[38]Sang Min Ji, a Pramod H. Borse, etc., Phys. Chem. Chem. Phys, 2005, 7, 13151.

[39]Z. Z. Zou, J. H. Ye, K. Sayama, H. Arakawa, Nature., 2001, 414, 625.

[40]S. X. Ouyang, H.Tong, N.Umezawa, J. H. Ye, et al. J. Am. Chem. Soc., 2012, 134 (4), 1974–1977

[41]H. G. Kim, D. W. Hwang, Y. G. Kim and J. S. Lee, Chem.Commun., 1999, 1077.

[42]D. W. Hwang, H. G. Kim, J. Kim, K. Y. Cha, Y. G. Kim and J. S. Lee, J. Catal., 2000, 193, 40.

[43]N. Ishizawa, F. Marumo, T. Kawamura, M. Kimura, Acta. Crystallographica B, 1982,24,1968.

[44] A. J. Cohen, P . Mori-Sanchez and W. T. Yang, Science, 2008, 321,792.

Figure Captions:

Figure.1. The XRD patterns of nitridized $Sr_2Nb_2O_7$ (N:0~6.18 wt%) .

Figure 2 UV-vis diffuse reflectance spectrum (a) and the calculated band gaps (b) of nitridized $Sr_2Nb_2O_7$ (N:0~6.18 wt%).

Figure 3 The schematic band structures of nitridized $Sr_2Nb_2O_7$ (N:0~6.18 wt%).

Figure 4 The simulated crystal structures of pure $Sr_2Nb_2O_7$ and $SrNbO_2N$.

Figure 5 DFT calculation of $Sr_2Nb_2O_7$ (a,b) and $SrNbO_2N$(c,d): energy band dispersion (a,c) and density of states(b,d).

Figure 6 (a) The XRD patterns of as-prepared samples, TEM images (b,c), and UV-vis diffuse reflectance spectrum (d) of Ag_3PO_4/SNON-1023.

Figure.7. The evolution rate of acetone (a) and CO_2 (b) over as-prepared composite photcatalysts.

Figure 8 Photocatalytic degradation of IPA under visible light irradiation (400nm<λ<800nm), the changes of concentration of IPA (a), the evolution rate of CO_2 (b)and acetone (c) over the Ag_3PO_4, SNON-1023 and Ag_3PO_4/SNON-1023 composite photocatalyst.

Figure 9 The VB -XPS spectra of Ag_3PO_4 and SNON-1023.

Figure 10 The Schematic band structure of Ag_3PO_4/SNON-1023 composite photocatalyst.

Table 1 The physical properties of nitridized $Sr_2Nb_2O_7$ at different temperature.

Samples with different nitridation temperatures	Nigtrogen amount (wt %)	Band gap (eV)	Ag_3PO_4/nitridized $Sr_2Nb_2O_7$ (mass ratio=1:1)	Surface area (m^2g^{-1})
$Sr_2Nb_2O_7$	0.00	3.96	-----	
SNON-873	0.01	3.42	Ag_3PO_4/SNON-873	3.06
SNON-923	0.04	3.06	Ag_3PO_4/SNON-923	1.89
SNON-973	1.51	2.23	Ag_3PO_4/SNON-973	2.81
SNON-1023	2.42	2.15	Ag_3PO_4/SNON-1023	3.01
SNON-1073	3.64	1.91	Ag_3PO_4/SNON-1073	2.27
SNON-1173	6.18	1.87	Ag_3PO_4/SNON-1113	2.13

Table 2 Nb-O Bond lengths and O-Nb-O bond angles of $SrNbO_2N$ and $Sr_2Nb_2O_7$

Material	Nb-O Bond length / Å	O-Nb-O bond angle / degree	
$SrNbO_2N$	2.029	90.00	
	(a-o) 1.95	(a-o-c) 89.63	(a-o-d) 85.85
	(b-o) 1.94	(a-o-e) 89.63	(a-o-f) 97.16
$Sr_2Nb_2O_7$	(c-o) 1.985	(b-o-c) 88.33	(b-o-d) 78.55
	(d-o) 2.25	(b-o-e) 88.33	(b-o-f) 98.75
	(e-o) 1.985	(c-o-d) 82.13	(d-o-e) 82.13
	(f-o) 1.85	(e-o-f) 97.83	(f-o-c) 97.83

Figure. 1

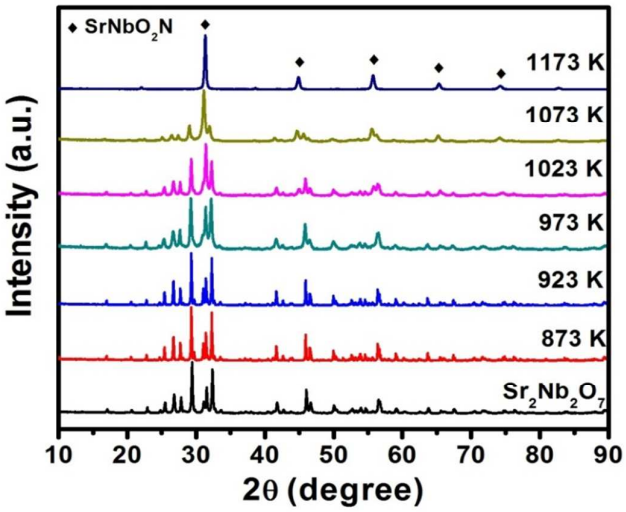

Figure. 2

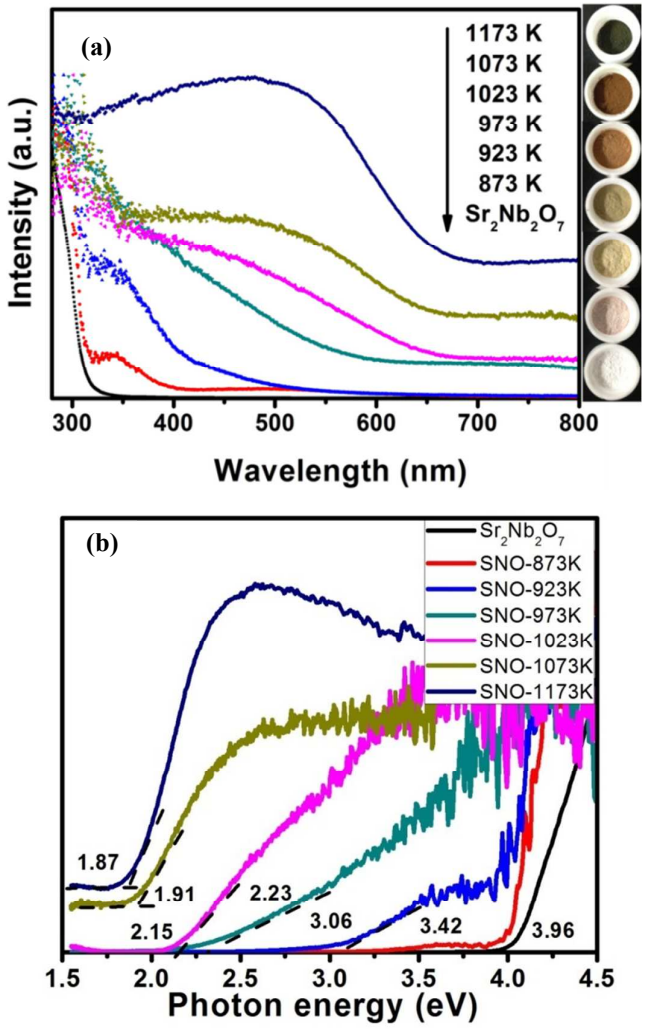

Figure. 3

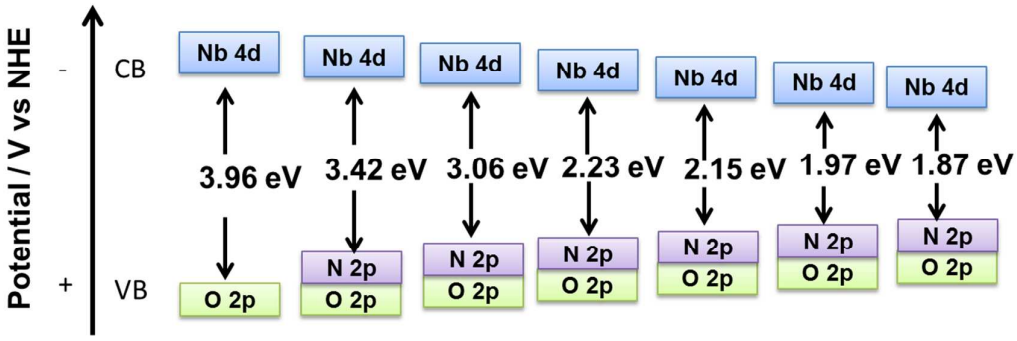

Figure. 4

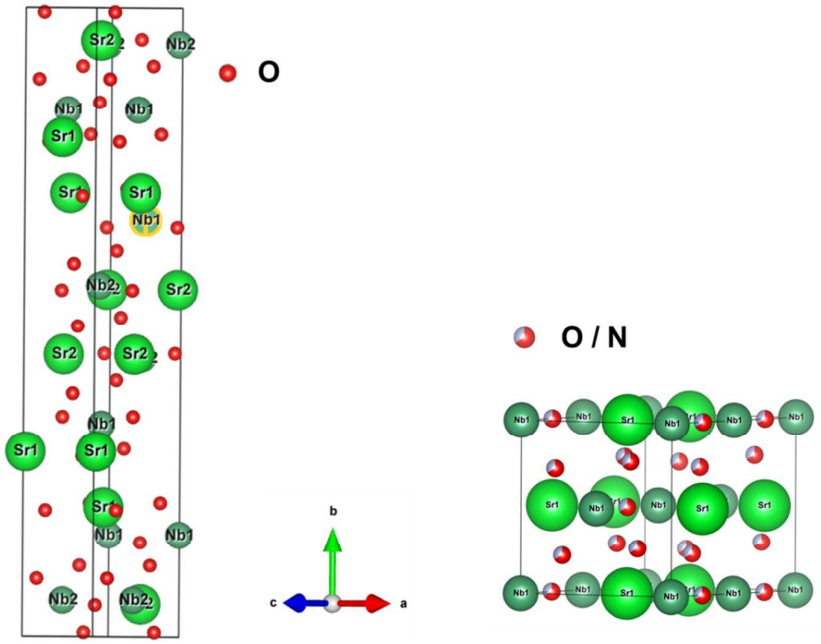

($Sr_2Nb_2O_7$) **($SrNbO_2N$)**

Figure. 5

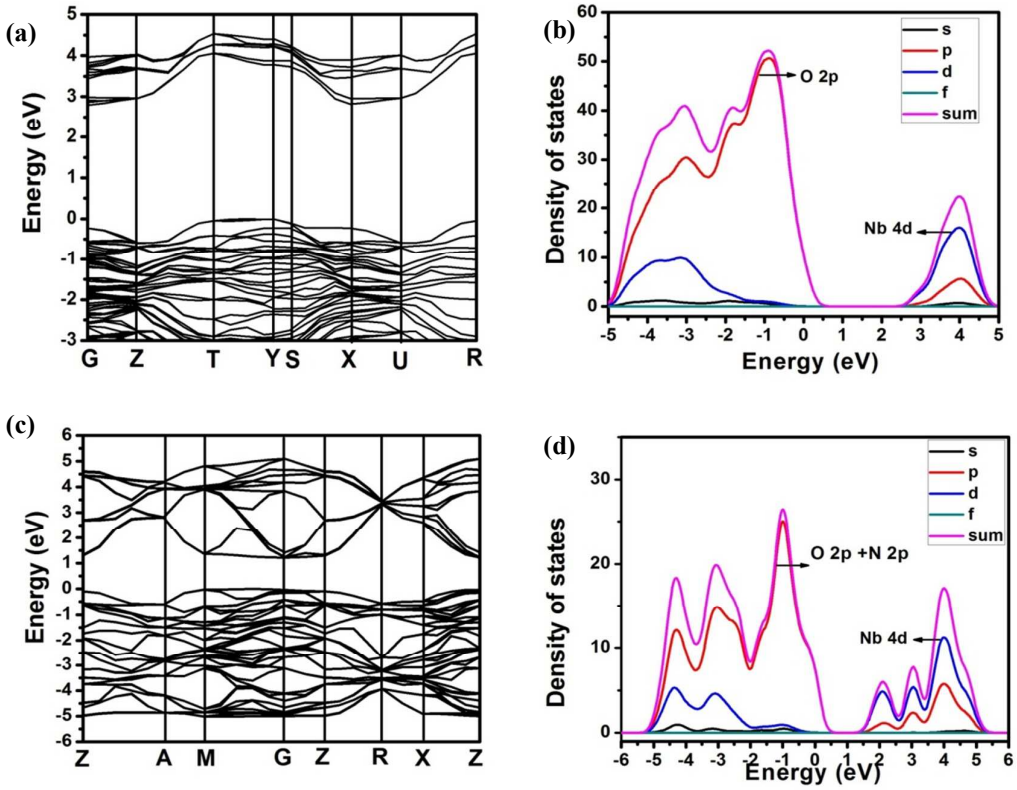

Figure. 6

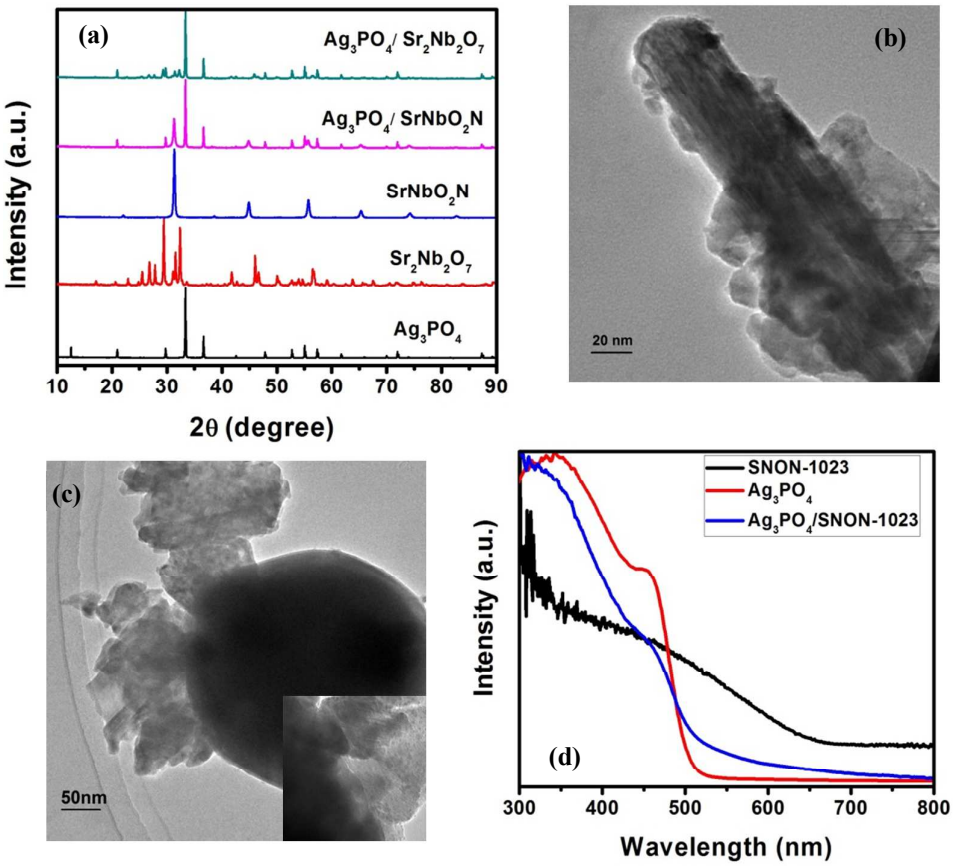

Figure. 7

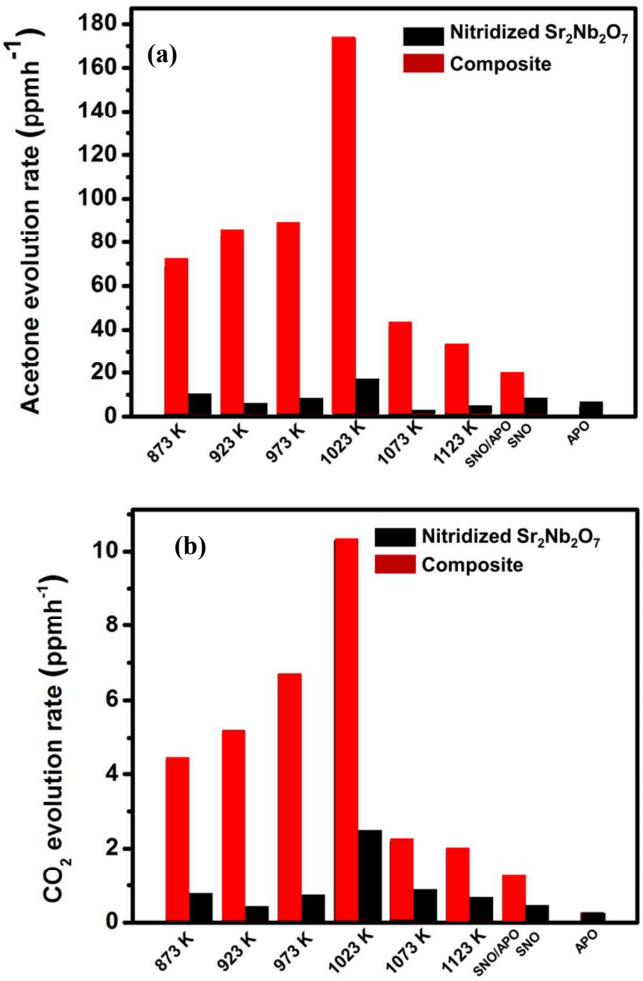

Figure. 8

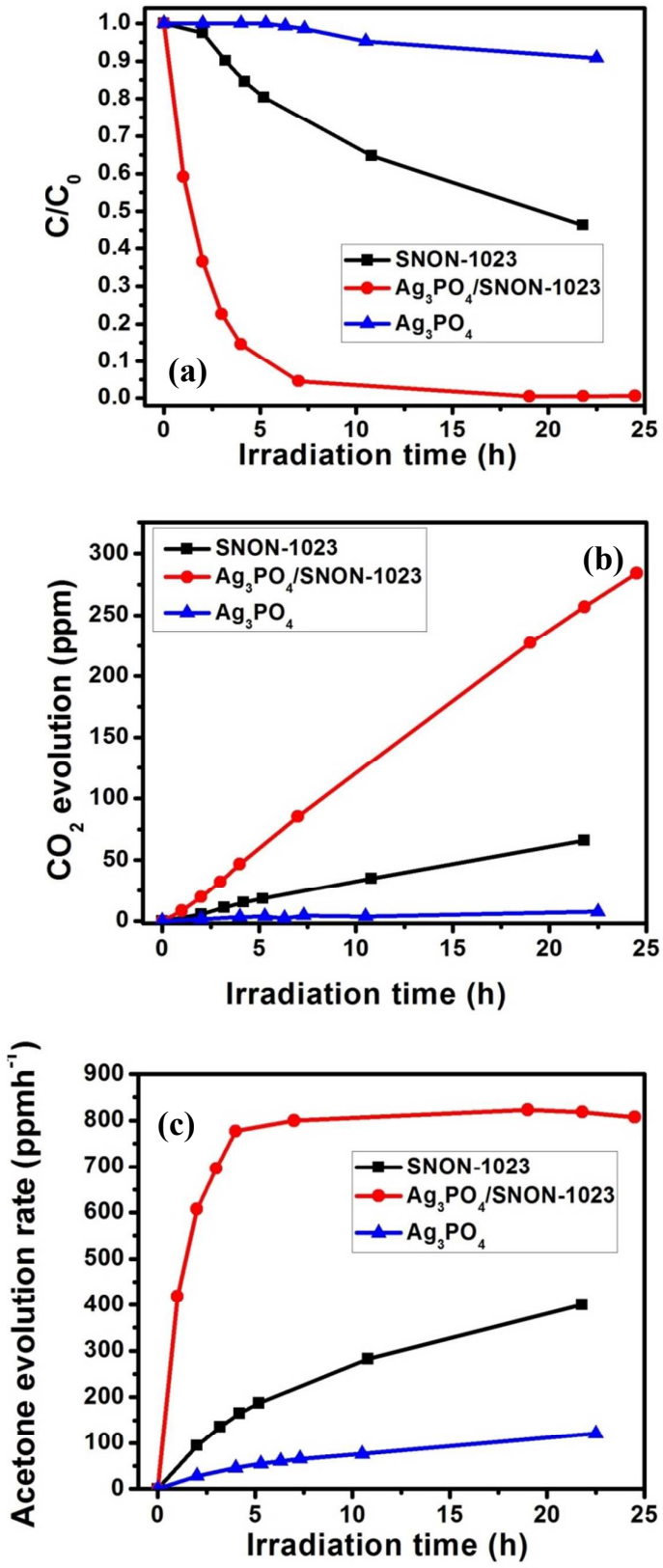

Figure. 9

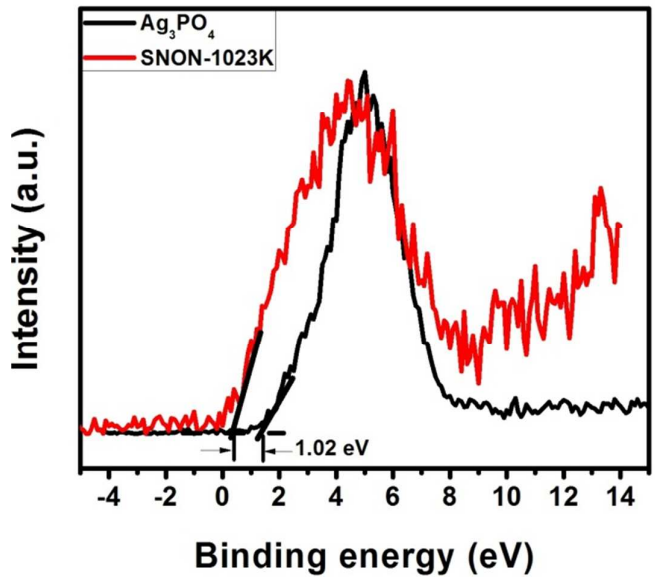

Figure.10